

pubs.acs.org/NanoLett Letter

# Polarization Control of Deterministic Single-Photon Emitters in Monolayer WSe<sub>2</sub>

Jae-Pil So,  $^{\nabla}$  Kwang-Yong Jeong,  $^{\nabla}$  Jung Min Lee,  $^{\nabla}$  Kyoung-Ho Kim, Soon-Jae Lee, Woong Huh, Ha-Reem Kim, Jae-Hyuck Choi, Jin Myung Kim, Yoon Seok Kim, Chul-Ho Lee, SungWoo Nam, and Hong-Gyu Park\*



Cite This: Nano Lett. 2021, 21, 1546-1554



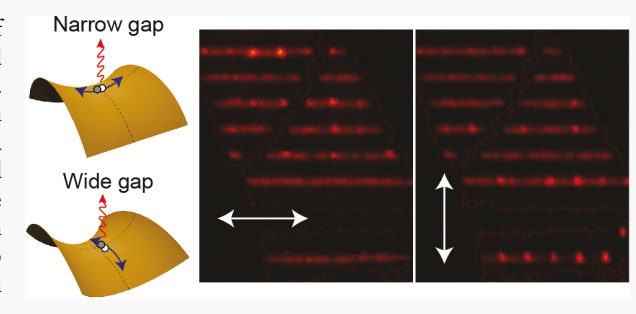
ACCESS

Metrics & More

Article Recommendations

s Supporting Information

**ABSTRACT:** Single-photon emitters, the basic building blocks of quantum communication and information, have been developed using atomically thin transition metal dichalcogenides (TMDCs). Although the bandgap of TMDCs was spatially engineered in artificially created defects for single-photon emitters, it remains a challenge to precisely align the emitter's dipole moment to optical cavities for the Purcell enhancement. Here, we demonstrate position- and polarization-controlled single-photon emitters in monolayer WSe<sub>2</sub>. A tensile strain of  $\sim 0.2\%$  was applied to monolayer WSe<sub>2</sub> by placing it onto a dielectric rod structure with a nanosized gap. Excitons were localized in the nanogap sites,



resulting in the generation of linearly polarized single-photon emission with a  $g^{(2)}$  of ~0.1 at 4 K. Additionally, we measured the abrupt change in polarization of single photons with respect to the nanogap size. Our robust spatial and polarization control of emission provides an efficient way to demonstrate deterministic and scalable single-photon sources by integrating with nanocavities.

KEYWORDS: single-photon emitter, polarization control, TMDC, cavity-coupled emitter

he single-photon source is one of the most important components in quantum information and quantum cryptography, promising highly secured processing of information without leakage. Solid-state single-photon emitters, such as semiconductor quantum dots,<sup>2,3</sup> and atomic defects in wide-bandgap materials 4-9 have attracted considerable attention because of the possibility of scaling quantum systems through wafer-scale growth and fabrication. 10,11 The performance of single-photon emitters can be improved by integrating them with well-designed optical cavities and increasing the Purcell factor. A high Purcell factor requires not only spatial and spectral matching but also polarization matching between the emitters and cavities. For example, several approaches have been employed including site-controlled growth, 15 high-energy ion implantation, 16,17 and high-power laser pulses 18 to control the position of singlephoton emitters, but these techniques still exhibited low yields.

More recently, quantum confinement in atomically thin transition metal dichalcogenides (TMDCs) has been investigated for single-photon emission based on naturally or artificially occurring defects. <sup>19–21</sup> In particular, it is feasible to precisely control the position of a single-photon emitter by applying mechanical strains to the TMDCs. <sup>22–29</sup> Strains have been induced in TMDCs using various nanostructures including dielectric pillars, <sup>23,24</sup> nanobubbles, <sup>25</sup> optical waveguide, <sup>26,27</sup> metal nanogaps, <sup>28</sup> and metal nanoparticles. <sup>29</sup>

However, increasing the Purcell factor through polarization control of emission and integration with a high-quality (Q) cavity remains elusive in TMDC-based single-photon sources. Although the polarization control of single-photon emission is critical for the Purcell enhancement, the polarization direction is generally uncontrolled in natural or strained defects of TMDCs, and thus the light emission is not efficiently coupled to a nanocavity.

The nanogap structures that induce anisotropic deformation in TMDCs unlike the nanopillars can be used to address this issue, because they can generate linearly polarized light<sup>28</sup> as well as provide mechanical stability during the transfer process of the optical cavity. In this work, we demonstrated deterministic control of the position and polarization of single-photon sources formed in monolayer WSe<sub>2</sub>. By applying a strain to monolayer WSe<sub>2</sub> using a Si<sub>3</sub>N<sub>4</sub> rod structure with a nanogap, band engineering and single-photon generation were successfully achieved at a desired position. Additionally, we

Received: January 7, 2021 Revised: January 24, 2021 Published: January 27, 2021





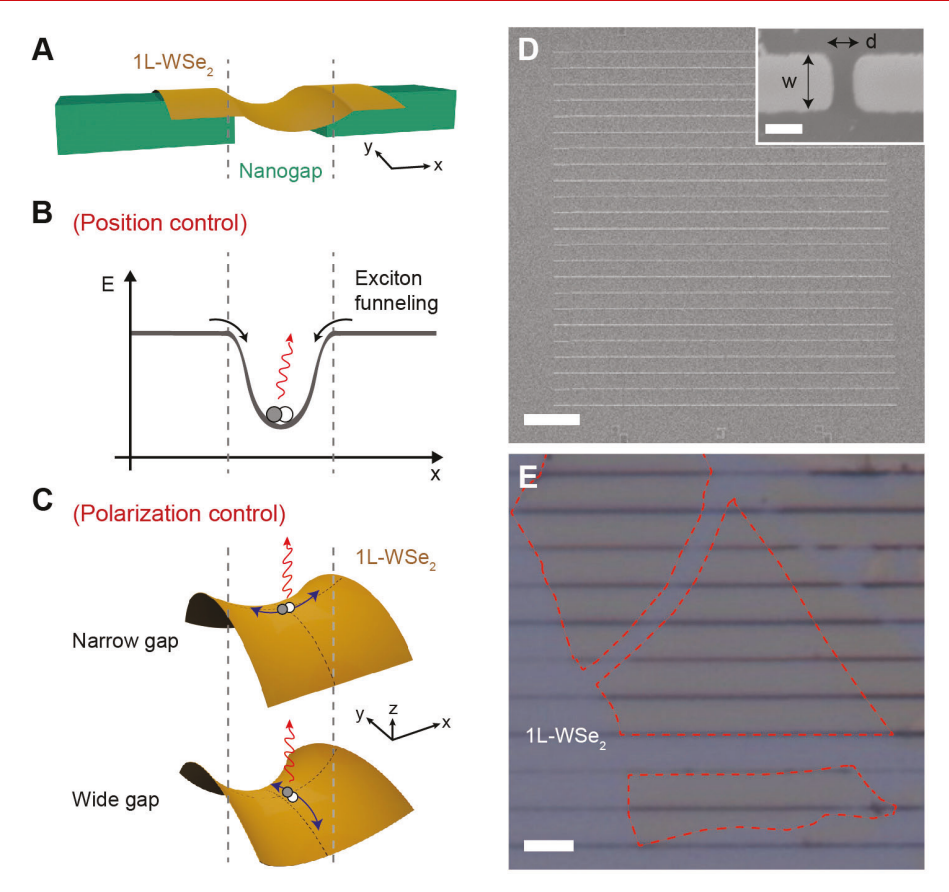


Figure 1. Single-photon source formed by gap strain. (A) Schematic of a single-photon source consisting of monolayer WSe<sub>2</sub> and the dielectric rod structure with a nanogap. (B) Schematic energy bandgap diagram along the x-axis in (A). The bandgap of WSe<sub>2</sub> is engineered by the strain at the nanogap site and a potential well is formed. Optically generated excitons funnel into the potential well and recombine for localized emission. (C) Schematics of the deformed monolayer WSe<sub>2</sub> due to the nanogap. The saddle-shaped deformation occurs along the x-axis (y-axis) for the narrow (wide) nanogap. The exciton oscillation is aligned with the elongation direction. (D) SEM image of the fabricated Si<sub>3</sub>N<sub>4</sub> rod structure array with nanogaps. The thickness of the Si<sub>3</sub>N<sub>4</sub> layer was 150 nm. Scale bar, 10  $\mu$ m. The inset shows a magnified SEM image of a nanogap (gap, d; width, w). Scale bar, 100 nm. (E) Optical microscope image captured after the monolayer WSe<sub>2</sub> flakes were transferred onto the Si<sub>3</sub>N<sub>4</sub> rod structures. The boundary of the monolayer WSe<sub>2</sub> is indicated by red dashed lines. Scale bar, 5  $\mu$ m.

controlled the polarization of single photons by changing the nanogap size. Numerical simulations were performed to elucidate the polarization control. Furthermore, we integrated the single-photon emitter with a photonic crystal nanobeam cavity to demonstrate a practical light source for quantum communication.

Figure 1A shows a schematic illustration of our singlephoton source. The monolayer WSe2 is placed on top of the dielectric rod structure with a nanogap that induces a local tensile strain. As shown in the schematic of the bandgap of WSe<sub>2</sub> (Figure 1B), the nanogap can generate a spatially modulated artificial trapping potential through a tensile straininduced perturbation of quantized energy states.<sup>30</sup> The excitons funnel into the manipulated states, implying position-controlled single-photon emission. This strain-tuned emitter at the nanogap site dominates the photoluminescence (PL) intensity at low temperatures because of the efficient exciton funneling from the unstrained surrounding region to the lower localized energy level.<sup>31</sup> Furthermore, our structure for single-photon emission allows control of its polarization in addition to its position. The saddle-shaped monolayer WSe<sub>2</sub> is formed at the nanogap site (Figure 1C). The dominant direction of elongation is defined according to the nanogap size: the monolayer WSe<sub>2</sub> is elongated along the x-axis (y-axis)

if the nanogap is relatively narrow (wide). The exciton oscillation occurs along the elongation axis.

To experimentally demonstrate the array of single-photon emitters, we first fabricated Si<sub>3</sub>N<sub>4</sub> rod structures with different gaps (d) and widths (w) on an  $SiO_2/Si$  substrate using electron-beam lithography and reactive ion etching (see Methods). Figure 1D shows a scanning electron microscope (SEM) image of the fabricated Si<sub>3</sub>N<sub>4</sub> rod structures. The value of d gradually changed from 60 nm (upper region) to 140 nm (lower region), whereas the value of w changed from 90 nm (left region) to 200 nm (right region). Different structural parameters of the nanogap can lead to different strains being applied to the monolayer WSe2 placed on the rod. Next, monolayer WSe2 flakes were transferred to the rod structures using the polydimethylsiloxane (PDMS) stamping method (see Methods). 32,33 As shown in an optical microscope image of the finished sample (Figure 1E), the monolayer WSe, flakes were successfully placed on the Si<sub>3</sub>N<sub>4</sub> rod structures. In addition, the atomic force microscope (AFM) images show the dominant direction of deformation depends on the nanogap size (Supporting Information Figure S1), as indicated by Figure 1C.

A two-dimensional confocal PL intensity map was generated to find single-photon emitters in the monolayer WSe, on the

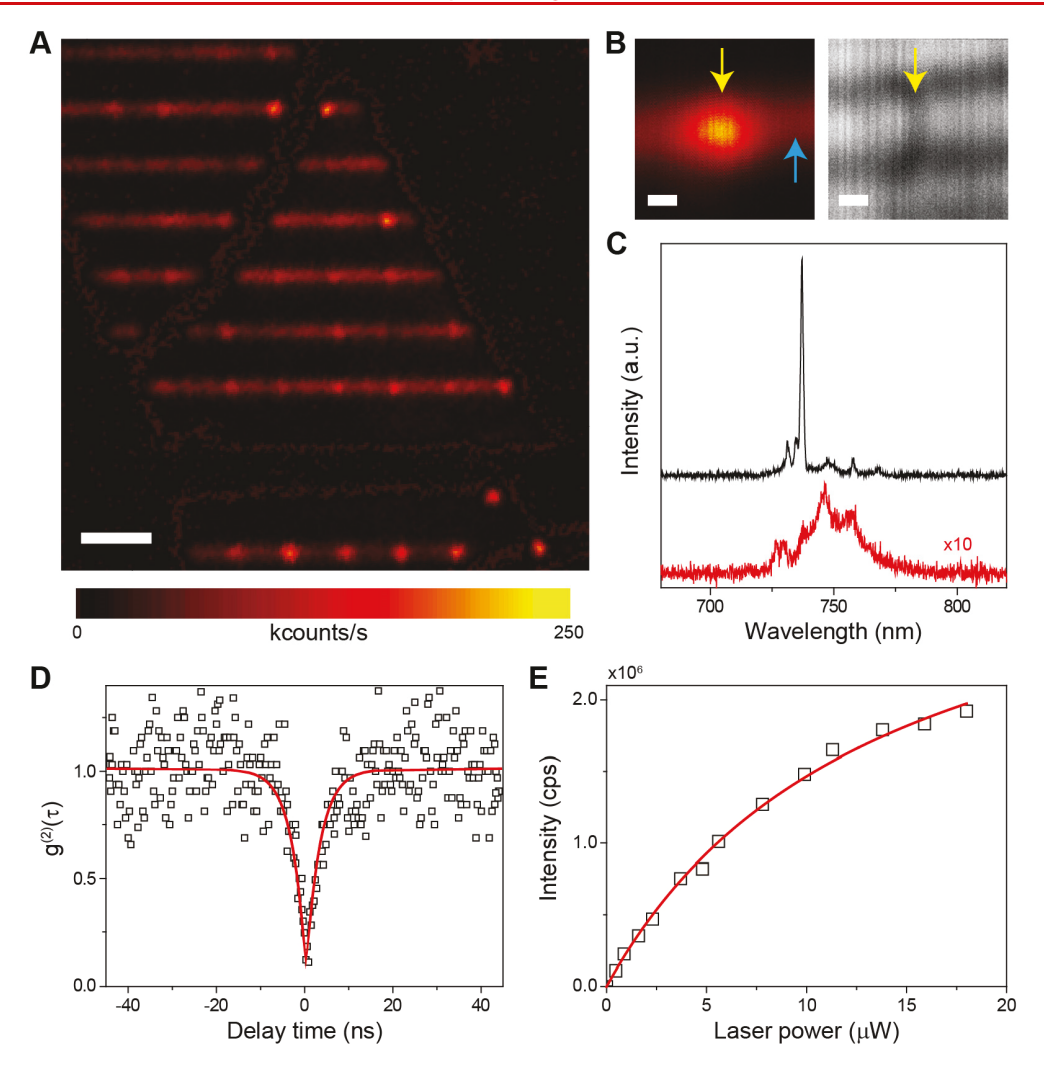


Figure 2. Measurement of single-photon emission. (A) Measured PL intensity map for the structure in Figure 1E. Localized photon emissions were observed at the nanogap sites. The pump power was 7.8  $\mu$ W. Scale bar, 5  $\mu$ m. (B) High-resolution raster scanning images of PL (left) and reflection (right) near the nanogap site. The yellow arrows were inserted for comparison of the positions of the emission spot and the nanogap. The pump power was 2.3  $\mu$ W for PL imaging. Scale bars, 100 nm. (C) PL spectra measured at the positions of the yellow and blue arrows in the PL image of (B) (black and red curves, respectively). (D) Measured photon correlation function  $g^{(2)}$  of the highest peak (at 737.19 nm) in the black curve of (C). The pump power was 1.8  $\mu$ W and a 10 nm wide spectral filter was used for the measurement. The fitted red curve indicates photon antibunching behavior with  $g^{(2)}(0) = 0.108 \pm 0.041$ . (E) Integrated PL intensity as a function of the pump laser power. A 10 nm wide spectral filter was used for the measurement. The fitted red curve indicates a saturation pump power of 13.7  $\mu$ W and a saturation emission intensity of 1.47 × 106 count/s.

rods with nanogaps. A high-resolution fast raster scan was performed using a continuous-wave pump laser with a wavelength of 532 nm and two scanning galvo mirrors. The light emission from the monolayer WSe<sub>2</sub> was collected by objective lens and sent to a monochromator/charge-coupled device (CCD) or avalanche photodiodes via optical fibers (see Methods and Supporting Information Figure S2). Additionally, a Hanbury Brown and Twiss (HBT) interferometer setup was constructed for the measurement of the second-order correlation. The temperature of the sample was varied from 4 K to room temperature.

Figure 2A shows the measured PL intensity map of the strained monolayer  $WSe_2$  at 4 K. Bright spots were observed at most of the nanogap sites of the  $Si_3N_4$  rod structures, which exhibited PL intensities >10 times stronger than those of the surrounding areas with no gaps. To clarify the emitting positions, we obtained the high-resolution image of a single

emission spot (Figure 2B, left) and compared it with a reflection image of the rod structure (Figure 2B, right). The positions of the bright spot and nanogap agreed very well; thus, the localized emission originated from the monolayer WSe<sub>2</sub> strained by the nanogap. Additionally, the PL spectra were measured at and near the nanogap (Figure 2C). The spectrum measured at the nanogap site (yellow arrow in Figure 2B) exhibited a strong emission peak at 737.19 nm with a subnanometer line width (<0.7 nm), whereas the measured PL spectrum was broad and weak for the rod with no gap (blue arrow in Figure 2B). We note that the submicron-sized localized emission spot ( $\sim$ 200 nm in size) and significant PL enhancement at the nanogap site were due to the exciton confinement resulting from the funneling effect.<sup>31</sup>

Next, to verify the single-photon feature of the emission, we measured the second-order correlation function  $g^{(2)}(\tau)$  of a strong emission peak using the HBT setup. In the PL spectrum

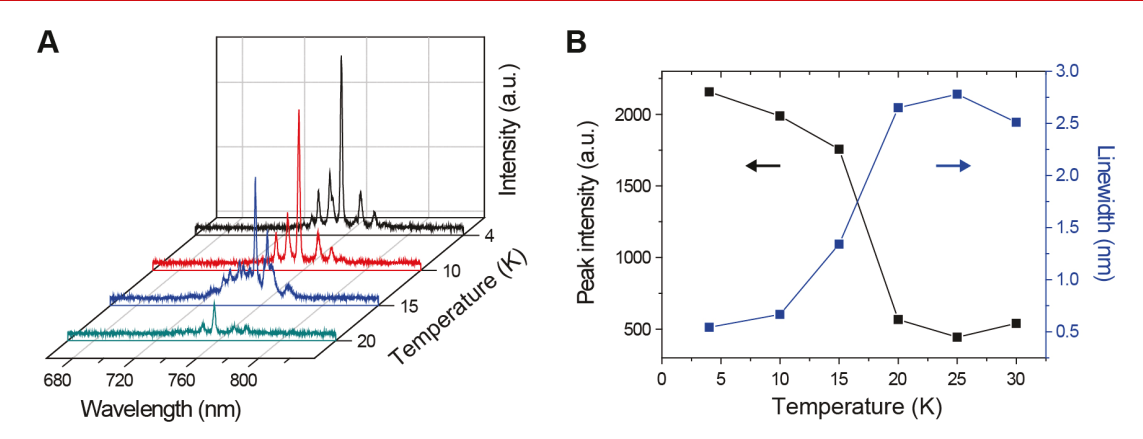


Figure 3. Temperature-dependent properties. (A) Measured PL spectra for the strained monolayer WSe<sub>2</sub> as functions of wavelength and temperature. The temperature varied from 4 to 20 K, and the pump power was 12.1  $\mu$ W. (B) Measured peak intensity (black) and spectral line width (blue) of the highest peak at a wavelength of 758 nm in (A), as a function of the temperature. Intensity suppression and line width broadening were observed above 20 K.

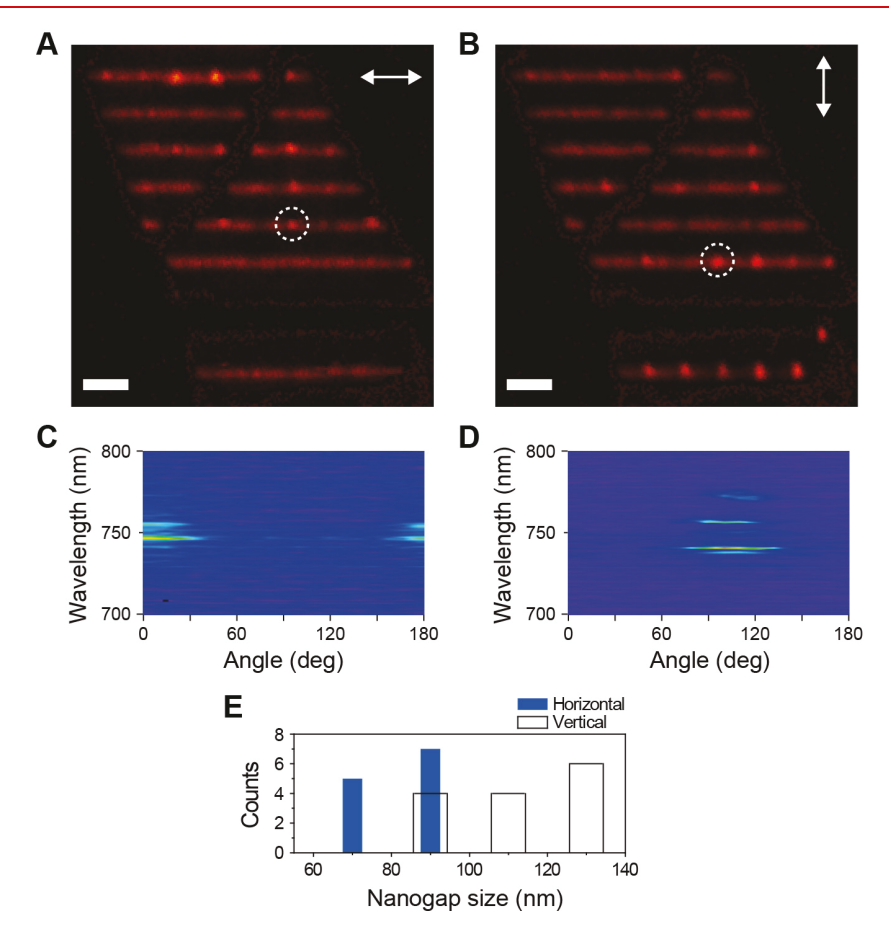


Figure 4. Polarization-resolved measurements. (A,B) PL intensity maps with horizontal (A) and vertical (B) polarization directions. Scale bars, 5  $\mu$ m. (C,D) Measured PL spectra as a function of the polarizer angle for the emitter positions indicated by the white dashed circles in panel A (C) and panel B (D). (E) Number of emitters with horizontal (blue) and vertical (white) polarization directions for each nanogap size.

of Figure 2C, a narrow spectral window was opened to select the sharp peak at 737.19 nm using a band-pass filter with a bandwidth of 10 nm.  $g^{(2)}(\tau)$  was measured (dots in Figure 2D) and fit with a three-level model (red line in Figure 2D). The value of  $g^{(2)}(0)$  was 0.108  $\pm$  0.041, which indicates photon antibunching. More  $g^{(2)}(0)$  values were measured from 0.045  $\pm$  0.030 to 0.133  $\pm$  0.044 at other nanogap sites (Supporting Information Figure S3). Additionally, we measured the

integrated PL intensity of the emission as a function of the pump power (Figure 2E). Intensity saturation was observed with a fitted saturation power of 13.7  $\mu$ W and an integrated intensity of 1.47  $\times$  10<sup>6</sup> counts/s at the saturation power.

To estimate the percentage of the nanogap sites showing single-photon emission with  $g^{(2)}(0) < 0.5$ , we measured  $g^{(2)}(\tau)$  from all nanogap sites covered with monolayer WSe<sub>2</sub> flake in three different samples (Figure 2 and Supporting Information

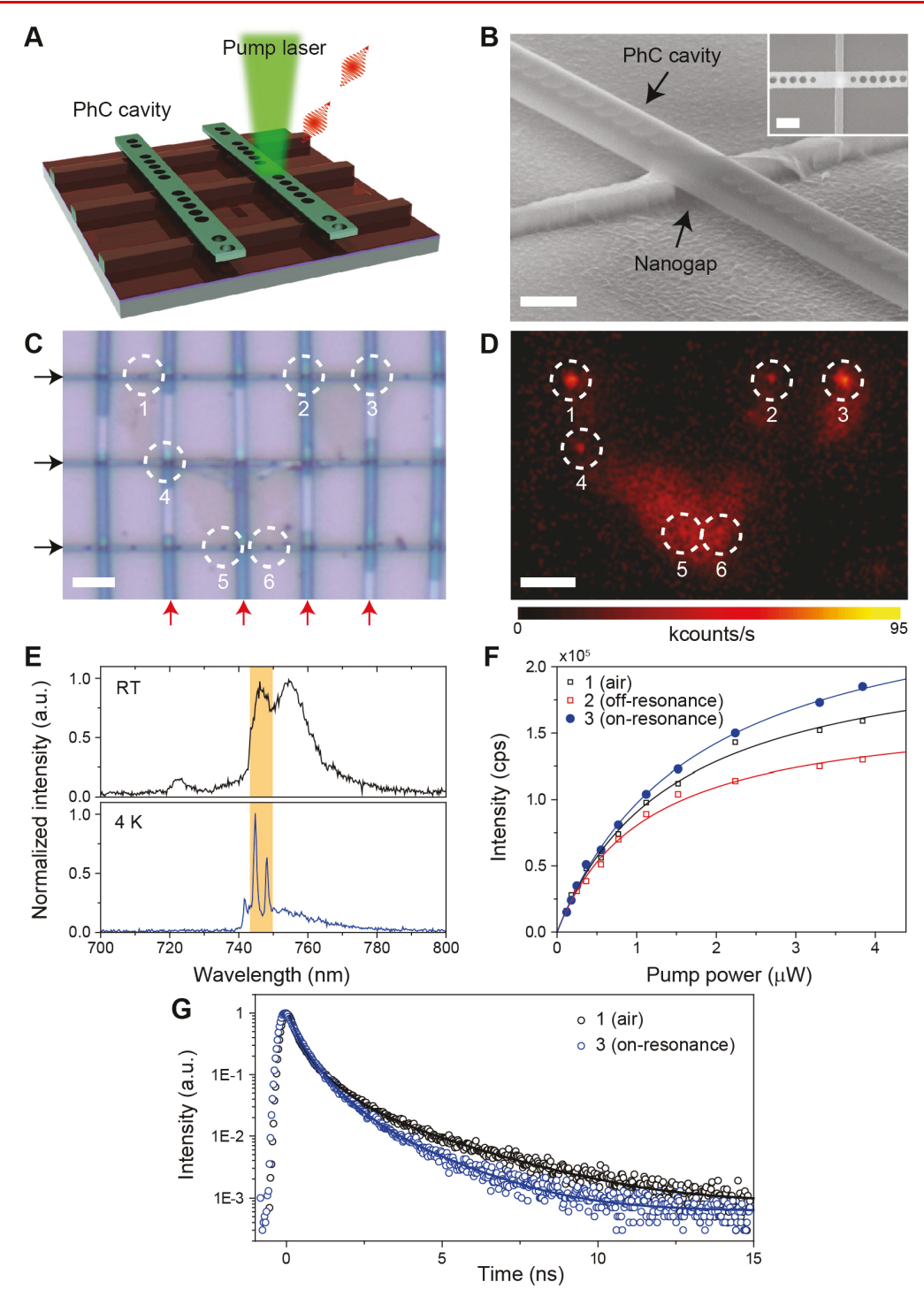


Figure 5. Cavity-coupled single-photon emitter. (A) Schematic of the single-photon emitters coupled to one-dimensional photonic crystal cavities. (B) SEM image of a fabricated cavity-coupled single-photon emitter. The photonic crystal cavity was transferred onto the nanogap. Scale bar, 500 nm. The inset shows the top-view SEM image. The photonic crystal cavity consists of three missing air holes in a one-dimensional nanobeam structure with a lattice constant of 280 nm, a regular hole diameter of 195 nm, and a reduced hole diameter of 95 nm. The slab thickness and width of the nanobeam structure were 200 and 420 nm, respectively. Scale bar, 500 nm. (C) Optical microscope image of the one-dimensional photonic crystal nanobeam cavity array transferred onto the  $Si_3N_4$  rod structure array with nanogaps and strained monolayer WSe<sub>2</sub>. The black and red arrows indicate the  $Si_3N_4$  rod structures and photonic crystal structures, respectively. Scale bar, 3  $\mu$ m. (D) High-resolution raster scanning PL image of (C). The pump power was  $1.12 \,\mu$ W for PL imaging. Scale bar, 3  $\mu$ m. (E) Measured PL spectra of Emitter 3 at room temperature (top) and at 4 K (bottom). The cavity mode peak was observed at 746.1 nm (orange box, top). (F) Measured PL intensities for Emitters 1 (black), 2 (red), and 3 (blue) as a function of the pump laser power. The fitted curves indicate saturation pump powers of 1.45 (black), 1.11 (red) and 1.74  $\mu$ W (blue), and saturation emission intensities of  $2.22 \times 10^5$  (black),  $1.70 \times 10^5$  (red), and  $2.67 \times 10^5$  count/s (blue). (G) Time-resolved PL measurements of Emitters 1 (black) and 3 (blue). The solid black and blue lines are fittings with decay times of  $3.67 \pm 0.09$  ns and  $1.95 \pm 0.13$  ns, respectively.

Figure S4). As a result, a clear single-photon feature was observed in 55 out of 66 nanogap sites. This yield of 83% is comparable to the yields in the previous reports ranging from 85% to 96%. <sup>23,24</sup>

We characterized other key properties of the single-photon emission at the nanogap sites. First, temperature-dependent PL spectra were measured while the sample temperature was varied from 4 to 20 K (Figure 3A). The intensities and numbers of peaks decreased with the increasing temperature. To investigate the temperature dependence of the peak indicating photon antibunching, we plotted the intensity and line width of the highest peak at a wavelength of 758 nm as a function of the temperature (Figure 3B). Above 20 K, the peak intensity decreased and the spectral line width increased significantly. This temperature-dependent behavior of singlephoton emission implies that the trapping potential of the localized excitons at the nanogap site was lower than the thermal energy ( $E_{\rm T} = k_{\rm B}T$ ) above the critical temperature of 20 K. The trapping potential can be estimated quantitatively based on the measured temperature dependence (Supporting Information Figure S5).<sup>34</sup> We obtained 1.93 meV (or 22.4 K) for the trapping potential, which agreed well with the measured critical temperature of 20 K.

Next, we examined the strains introduced by the nanogap, by measuring the PL spectrum at room temperature (Supporting Information Figure S6A). The wavelength of light emission at the nanogap site was red-shifted by ~6–8 nm versus background because of the nanogap site-induced reduction of the bandgap of WSe<sub>2</sub>. The bandgap reduction was between 12.7 to 17.9 meV, which corresponds to an applied tensile strain between 0.26% and 0.36% (Supporting Information Figure S6B,C). A strain of 0.16% was applied to the Si<sub>3</sub>N<sub>4</sub> rod structure with no gap. The strain difference between the nanogap and the surroundings led to the formation of a potential well, giving rise to the funneling effect (see Figure 1B), when the thermal fluctuation was less than the potential well. We believe that this is the first observation to confirm that a small strain of ~0.2% can generate a potential well of sufficient depth, resulting in single-photon emission.

We investigated the polarization of the single-photon emission at nanogap sites. To this end, the polarizationresolved PL intensity maps were measured using a linear polarizer placed in front of the detector (Figure 4A,B). The sample of Figure 2A was examined first. Interestingly, each single-photon source was polarized either along or across the axis of the Si<sub>3</sub>N<sub>4</sub> rod structure, which corresponds to the horizontal and vertical polarization directions, respectively. In particular, the horizontally polarized emission was observed in the upper region of the sample with relatively narrow nanogaps (Figure 4A), whereas the vertically polarized emission was observed in the lower region of the sample with relatively wide nanogaps (Figure 4B). Figure 4C shows the measured polarization from the single-photon emitter marked by the white dashed circle in Figure 4A. The nanogap size was 90 nm at this site. Indeed, linearly polarized emissions along the horizontal direction (0° or 180°) were dominantly observed; the degree of polarization at the strongest peak was 0.928. Additionally, we measured the polarization from the singlephoton emitter at a nanogap with a size of 110 nm (white dashed circle in Figure 4B). The vertical polarization direction (90°) was dominantly observed with a degree of polarization of 0.962 (Figure 4D). The polarization distribution of the 26

single-photon emitters was plotted with respect to the nanogap size (Figure 4E). This graph clearly indicated that the polarization direction changed depending on whether the nanogap was larger or smaller than 90 nm. We note additional characteristics of the emission in these measurement results. First, the single-photon features of narrow peaks and photon antibunching were not observed when the nanogap was larger than 130 nm. Second, the width of the rod structure did not affect the polarization state. Third, the emitters always showed a single linear polarization peak, as observed in the previous reports. <sup>20,28,38,39</sup> The elimination of the electron—hole exchange occurred possibly due to the anisotropic strain at the nanogap site. <sup>28</sup>

We measured polarization-resolved PL intensity maps for two additional samples (Supporting Information Figure S4). Similar to Figure 4, the polarization direction strongly depended on the nanogap size. When the nanogap was smaller or larger than a critical value, horizontal or vertical polarization was observed, respectively; the critical value of the nanogap size was 80 nm for Figure S4A,C and 90 nm for Figure S4B,D. Therefore, our results show that we can control the polarization of single photons by simply changing the size of the nanogap exerting strain on the monolayer WSe<sub>2</sub>.

The dependence of the polarization direction on the nanogap size is explained by the saddle-shaped anisotropic deformation of the monolayer WSe<sub>2</sub>, as shown in Figure 1C. Single-photon emission was observed only when monolayer WSe2 flakes were transferred onto the rod structures using an all-dry PDMS stamping method. 32,33 No single-photon feature was observed when the conventional solution-based transfer method was used. The results of the experiment indicated that the pressure of the PDMS stamp could cause strain on the WSe2 at the nanogap sites. To support this explanation, we simulated the morphology of the PDMS pressed onto the narrow (60 nm) or wide (140 nm) nanogap using the finiteelement method (FEM) (see Methods). The simulation results indicated that two types of saddle-shaped deformation occurred in the PDMS, depending on the nanogap size (Supporting Information Figure S7A,B). To investigate the deformation morphology, we examined the cross-sectional profiles along the x-axis (black dashed lines in Figure S7A,B) and y-axis (white dashed lines in Figure S7A,B). In the case of the narrow nanogap (Supporting Information Figure S7C), the y-axis deformation of the PDMS (red) was significantly larger than the x-axis deformation of the PDMS (black). However, for the wide nanogap, the x-axis deformation was dominant (Supporting Information Figure S7D). Assuming that the morphology of the monolayer WSe2 will follow that of the PDMS after the transfer process, our final WSe<sub>2</sub> morphology will exhibit anisotropic strains, resulting in gap-dependent exciton localization and two different polarization directions of single photons.

To improve the performance of the single-photon emitters, it is necessary to integrate the emitters with an optical cavity for enhancement of the Purcell factor.  $^{12-14}$  Our single-photon emitters in strained monolayer  $WSe_2$  allow for adjustment of the polarization and position, making it easy to combine with nanocavities. For example, a one-dimensional photonic crystal cavity can be integrated with the  $Si_3N_4$  rod structure by constructing an orthogonal structure (90° to each other) (Figure 5A). The nanogap of the emitter and the no-air-hole defect region of the photonic crystal cavity are well matched in position; thus, the single-photon emitter at the nanogap site

can be coupled to the cavity. Indeed, we successfully fabricated the cavity-coupled single-photon emitters by transferring the designed cavities onto strained monolayer WSe<sub>2</sub> using the transfer printing method (Figure 5B and Methods).<sup>40</sup> The topview SEM image shows that the defect region of the photonic crystal nanobeam cavity was placed on top of the nanogap of the Si<sub>2</sub>N<sub>4</sub> rod structure (inset of Figure 5B).

We transferred the one-dimensional photonic crystal nanobeam cavity array onto the Si<sub>3</sub>N<sub>4</sub> rod structure array with nanogaps and strained monolayer WSe2 (Figure 5C) and characterized nanocavity-coupled PL emission (Figure 5D). The single photons emitted at the nanogaps were designed to be well-coupled to the photonic crystal nanobeam cavities: the polarization direction of the emitted single photons is along the axis of the Si<sub>3</sub>N<sub>4</sub> rod structure by fabricating narrow nanogaps with ~80 nm, whereas the polarization of the cavity mode is perpendicular to the axis of the photonic crystal nanobeam cavity (Supporting Information Figure S8). Among six single-photon emitters (Supporting Information Figure S9A), three (Emitters 1, 5, and 6) were uncoupled and the other three (Emitters 2, 3, and 4) were coupled to photonic crystal nanobeam cavities (Figure 5C). Figure 5D shows the measured PL intensity map of this sample at 4 K. Emitter 3 was observed to be brighter than the other emitters.

To further investigate the optical properties of Emitter 3, we first measured room-temperature PL, which shows only the resonance feature of the photonic crystal nanobeam cavity. The cavity mode peak was observed at 746.1 nm, showing a Q factor of  $\sim 170$  (orange box in the top panel, Figure 5E). With the consideration of the calculated mode volume of the photonic crystal cavity, 0.82  $(\lambda/n)^3$ , where  $\lambda$  is the resonant wavelength and n is the refractive index of  $Si_3N_4$ , we estimate the Purcell factor of ~15.8 when the emitter is spectrally and spatially matched to the cavity mode. 41,42 We note that the Purcell factor significantly decreases when the nanogap is placed at the intensity node of the cavity mode that is 100 nm away from the center (Supporting Information Figure S10). The resolution of our transfer printing method is ∼100 nm but in order to reproducibly obtain a high Purcell factor, it would be necessary to develop a transfer technique with a resolution smaller than 100 nm.

The comparison between the PL spectra measured at room temperature and 4 K shows that this single-photon emitter is spectrally well-matched to the cavity mode (Figure 5E). Emitter 3 also exhibited photon antibunching behavior with linearly polarized direction along the Si<sub>3</sub>N<sub>4</sub> rod structure (Supporting Information Figure S9B,C). This measurement demonstrates polarization matching between the single-photon emitter and the cavity mode. Notably, the saturation emission intensity quantitatively shows that Emitter 3 is brighter than the uncoupled emitter (Emitter 1) or off-resonance coupled emitter (Emitter 2), as a result of the on-resonance coupling of Emitter 3 with the photonic crystal nanobeam cavity (Figure 5F). We included the emission intensity of the uncoupled emitter (Emitter 1) as a reference to compare with coupled Emitter 3, because the fabrication conditions (e.g., pressure of the PDMS stamp for transfer process and the fabricated Si<sub>3</sub>N<sub>4</sub> rod structures) might be different among different samples.

Furthermore, we performed time-resolved PL measurements of these emitters (see Methods). Figure 5G shows that the decay time of Emitter 3 is  $1.95 \pm 0.13$  ns, which is reduced to approximately half of that of Emitter 1. This result clearly demonstrates the Purcell enhancement of the emitter coupled

with a cavity. In addition, the Purcell factor can be estimated using the enhancement of the radiative decay rate due to the coupling with a cavity.  $^{29,43}$  The measured decay curves in our work were well fitted with a single exponential, which indicated relatively high internal quantum efficiency. Also, the dielectric photonic crystal nanobeam cavity is expected not to bring additional nonradiative losses. By comparing the coupled emitter (Emitter 3) and uncoupled emitter (Emitter 1), the Purcell factor is estimated to be  $\sim$ 1.88. We note that this value is lower than the value obtained using the Q factor and mode volume possibly due to imperfect spatial matching between the emitter and the cavity (Supporting Information Figure S10).

Therefore, we believe that our experiment will help facilitate the demonstration of a scalable and integrable single-photon source array. In addition, although the cavity was purposely designed to have a relatively low Q factor in order to account for uncertainty in the emission wavelength of the emitter, Q can be further increased by the optimization of the structure, for example, by using a  $SiO_2$  rod structure underneath the cavity (Supporting Information Figure S11), and the cavity coupling performance can be improved.

In summary, we demonstrated deterministic control of both the position and polarization of single-photon emitters in atomically thin WSe<sub>2</sub> placed on a nanogap array. Manipulation of the band structure by a local strain gradient generated a trapping potential at the nanogap site, and position-controlled single-photon emission was subsequently achieved. Additionally, directional elongations of the potential well, which were tuned by changing the nanogap size, allowed polarizationcontrolled single-photon emission. Moreover, single photons with a g $^{(2)}$  of  $\sim 0.1$  were generated at 4–20 K. To take a full advantage of such deterministic control of the position and polarization of single-photon emitters, we successfully integrated the emitters with one-dimensional photonic crystal nanobeam cavities. We believe that our approach is a unique way to develop next-generation, deterministic, controllable single-photon emitters based on TMDC materials, which outperform the present single-photon sources with random occurrence and uncontrolled polarization properties.

## ASSOCIATED CONTENT

## Supporting Information

The Supporting Information is available free of charge at https://pubs.acs.org/doi/10.1021/acs.nanolett.1c00078.

Detailed description of experimental/simulation methods and additional figures (PDF)

## AUTHOR INFORMATION

### **Corresponding Authors**

SungWoo Nam — Department of Materials Science and Engineering, University of Illinois at Urbana-Champaign, Champaign, Illinois 61801, United States; Department of Mechanical Science and Engineering, University of Illinois at Urbana-Champaign, Champaign, Illinois 61801, United States; ⊚ orcid.org/0000-0002-9719-7203;

Email: swnam@illinois.edu

Hong-Gyu Park — Department of Physics and KU-KIST Graduate School of Converging Science and Technology, Korea University, Seoul 02841, Republic of Korea; Center for Molecular Spectroscopy and Dynamics, Institute for Basic Science, Seoul 02841, Republic of Korea; Ocid.org/0000-0002-6375-0314; Email: hgpark@korea.ac.kr

#### **Authors**

- Jae-Pil So Department of Physics, Korea University, Seoul 02841, Republic of Korea
- Kwang-Yong Jeong Department of Physics, Korea University, Seoul 02841, Republic of Korea
- Jung Min Lee Department of Physics, Korea University, Seoul 02841, Republic of Korea
- Kyoung-Ho Kim Department of Physics, Chungbuk National University, Cheongju 28644, Republic of Korea Soon-Jae Lee — Department of Physics, Korea University,
- Seoul 02841, Republic of Korea Woong Huh – KU-KIST Graduate School of Converging Science and Technology, Korea University, Seoul 02841, Republic of Korea
- Ha-Reem Kim Department of Physics, Korea University, Seoul 02841, Republic of Korea
- Jae-Hyuck Choi Department of Physics, Korea University, Seoul 02841, Republic of Korea
- Jin Myung Kim Department of Materials Science and Engineering, University of Illinois at Urbana-Champaign, Champaign, Illinois 61801, United States
- Yoon Seok Kim KU-KIST Graduate School of Converging Science and Technology, Korea University, Seoul 02841, Republic of Korea
- Chul-Ho Lee KU-KIST Graduate School of Converging Science and Technology and Department of Integrative Energy Engineering, Korea University, Seoul 02841, Republic of Korea; orcid.org/0000-0003-1570-8688

Complete contact information is available at: https://pubs.acs.org/10.1021/acs.nanolett.1c00078

## **Author Contributions**

 $^{
m V}$ J.-P.S. K.-Y.J., and J.M.L. contributed equally to this work.

The authors declare no competing financial interest.

## ACKNOWLEDGMENTS

This work was supported by the Institute for Information & Communications Technology Promotion (IITP) Grants (2017-0-00575 and 2020-0-00841), the National Research Foundation of Korea (NRF) grant funded by the Korean government (MSIT) (2018R1A3A3000666 and 2020R1A4A2002828), the Samsung Research Funding & Incubation Center of Samsung Electronics (SRFC-MA2001-01), and IBS-R023-D1. S.N. acknowledges the support from the AFOSR FA2386-17-1-4071 and NSF MRSEC DMR-1720633. C.-H.L. acknowledges the support from the NRF of Korea (2020M3H3A1105796) and the KU-KIST School Project. K.-Y.J. acknowledges the support from the NRF of Korea (2020R1I1A1A01066655).

## REFERENCES

- (1) Lo, H.-K.; Curty, M.; Tamaki, K. Secure quantum key distribution. *Nat. Photonics* **2014**, *8*, 595–604.
- (2) Michler, P.; Imamoglu, A.; Mason, M. D.; Carson, P. J.; Strouse, G. F.; Buratto, S. K. Quantum correlation among photons from a single quantum dot at room temperature. *Nature* **2000**, *406*, 968–970
- (3) Santori, C.; Fattal, D.; Vuckovic, J.; Solomon, G. S.; Yamamoto, Y. Indistinguishable photons from a single-photon device. *Nature* **2002**, *419*, 594–597.

- (4) Zhou, Y.; Rasmita, A.; Li, K.; Xiong, Q.; Aharonovich, I.; Gao, W. Coherent control of a strongly driven silicon vacancy optical transition in diamond. *Nat. Commun.* **2017**, *8*, 14451.
- (5) Lovchinsky, I.; Sanchez-Yamagishi, J. D.; Urbach, E. K.; Choi, S.; Fang, S.; Andersen, T. I.; Watanabe, K.; Taniguchi, T.; Bylinskii, A.; Kaxiras, E.; Kim, P.; Park, H.; Lukin, M. D. Magnetic resonance spectroscopy of an atomically thin material using a single-spin qubit. *Science* **2017**, *355*, 503–507.
- (6) Berhane, A. M.; Jeong, K.-Y.; Bodrog, Z.; Fiedler, S.; Schröder, T.; Trivino, N. V.; Palacios, T.; Gali, A.; Toth, M.; Englund, D.; Aharonovich, I. Bright Room-Temperature Single-Photon Emission from Defects in Gallium Nitride. *Adv. Mater.* **2017**, *29*, 1605092.
- (7) Grosso, G.; Moon, H.; Lienhard, B.; Ali, S.; Efetov, D. K.; Furchi, M. M.; Jarillo-Herrero, P.; Ford, M. J.; Aharonovich, I.; Englund, D. Tunable and high-purity room temperature single-photon emission from atomic defects in hexagonal boron nitride. *Nat. Commun.* **2017**, 8, 705
- (8) Tran, T. T.; Elbadawi, C.; Totonjian, D.; Lobo, C. J.; Grosso, G.; Moon, H.; Englund, D. R.; Ford, M. J.; Aharonovich, I.; Toth, M. Robust Multicolor Single Photon Emission from Point Defects in Hexagonal Boron Nitride. *ACS Nano* **2016**, *10*, 7331–7338.
- (9) Aharonovich, I.; Englund, D.; Toth, M. Solid-state single-photon emitters. *Nat. Photonics* **2016**, *10*, 631–641.
- (10) Sollner, I.; Mahmoodian, S.; Hansen, S. L.; Midolo, L.; Javadi, A.; Kirsanske, G.; Pregnolato, T.; El-Ella, H.; Lee, E. H.; Song, J. D.; Stobbe, S.; Lodahl, P. Deterministic photon–emitter coupling in chiral photonic circuits. *Nat. Nanotechnol.* **2015**, *10*, 775–778.
- (11) Zhang, C.; Zhao, S.; Jin, C.; Koh, A. L.; Zhou, Y.; Xu, W.; Li, Q.; Xiong, Q.; Peng, H.; Liu, Z. Direct growth of large-area graphene and boron nitride heterostructures by a co-segregation method. *Nat. Commun.* **2015**, *6*, 6519.
- (12) Badolato, A.; Hennessy, K.; Atatüre, M.; Dreiser, J.; Hu, E.; Petroff, P. M.; Imamoglu, A. Deterministic Coupling of Single Quantum Dots to Single Nanocavity Modes. *Science* **2005**, *308*, 1158–1161.
- (13) Tran, T. T.; Wang, D.; Xu, Z.-Q.; Yang, A.; Toth, M.; Odom, T. W.; Aharonovich, I. Deterministic Coupling of Quantum Emitters in 2D Materials to Plasmonic Nanocavity Arrays. *Nano Lett.* **2017**, *17*, 2634–2639.
- (14) Iff, O.; Lundt, N.; Betzold, S.; Tripathi, L. N.; Emmerling, M.; Tongay, S.; Lee, Y. J.; Kwon, S.-H.; Höfling, S.; Schneider, C. Deterministic coupling of quantum emitters in WSe<sub>2</sub> monolayers to plasmonic nanocavities. *Opt. Express* **2018**, *26*, 25944–25951.
- (15) Schneider, C.; Strauss, M.; Sünner, T.; Huggenberger, A.; Wiener, D.; Reitzenstein, S.; Kamp, M.; Höfling, S.; Forchel, A. Lithographic alignment to site-controlled quantum dots for device integration. *Appl. Phys. Lett.* **2008**, *92*, 183101.
- (16) Schröder, T.; Walsh, M.; Zheng, J.; Mouradian, S.; Li, L.; Malladi, G.; Bakhru, H.; Lu, M.; Stein, A.; Heuck, M.; Englund, D. Scalable fabrication of coupled NV center photonic crystal cavity systems by self-aligned N ion implantation. *Opt. Mater. Express* **2017**, 7, 1514–1524.
- (17) Schroder, T.; Trusheim, M. E.; Walsh, M.; Li, L.; Zheng, J.; Schukraft, M.; Sipahigil, A.; Evans, R. E.; Sukachev, D. D.; Nguyen, C. T.; Pacheco, J. L.; Camacho, R. M.; Bielejec, E. S.; Lukin, M. D.; Englund, D. Scalable focused ion beam creation of nearly lifetime-limited single quantum emitters in diamond nanostructures. *Nat. Commun.* **2017**, *8*, 15376.
- (18) Chen, Y.-C.; Salter, P. S.; Knauer, S.; Weng, L.; Frangeskou, A. C.; Stephen, C. J.; Ishmael, S. N.; Dolan, P. R.; Johnson, S.; Green, B. L.; Morley, G. W.; Newton, M. E.; Rarity, J. G.; Booth, M. J.; Smith, J. M. Laser writing of coherent colour centres in diamond. *Nat. Photonics* **2017**, *11*, 77–80.
- (19) Srivastava, A.; Sidler, M.; Allain, A. V.; Lembke, D. S.; Kis, A.; Imamoglu, A. Optically active quantum dots in monolayer WSe<sub>2</sub>. *Nat. Nanotechnol.* **2015**, *10*, 491–496.
- (20) He, Y.-M.; Clark, G.; Schaibley, J. R.; He, Y.; Chen, M.-C.; Wei, Y.-J.; Ding, X.; Zhang, Q.; Yao, W.; Xu, X.; Lu, C.-Y.; Pan, J.-W. Single

- quantum emitters in monolayer semiconductors. *Nat. Nanotechnol.* **2015**, *10*, 497–502.
- (21) Tonndorf, P.; Schmidt, R.; Schneider, R.; Kern, J.; Buscema, M.; Steele, G. A.; Castellanos-Gomez, A.; van der Zant, H. S. J.; Michaelis de Vasconcellos, S.; Bratschitsch, R. Single-photon emission from localized excitons in an atomically thin semiconductor. *Optica* **2015**, *2*, 347–352.
- (22) Kumar, S.; Kaczmarczyk, A.; Gerardot, B. D. Strain-Induced Spatial and Spectral Isolation of Quantum Emitters in Mono- and Bilayer WSe<sub>2</sub>. *Nano Lett.* **2015**, *15*, 7567–7573.
- (23) Palacios-Berraquero, C.; Kara, D. M.; Montblanch, A. R.-P.; Barbone, M.; Latawiec, P.; Yoon, D.; Ott, A. K.; Loncar, M.; Ferrari, A. C.; Atature, M. Large-scale quantum-emitter arrays in atomically thin semiconductors. *Nat. Commun.* **2017**, *8*, 15093.
- (24) Branny, A.; Kumar, S.; Proux, R.; Gerardot, B. D Deterministic strain-induced arrays of quantum emitters in a two-dimensional semiconductor. *Nat. Commun.* **2017**, *8*, 15053.
- (25) Shepard, G. D.; Ajayi, O. A.; Li, X.; Zhu, X.-Y.; Hone, J.; Strauf, S. Nanobubble induced formation of quantum emitters in monolayer semiconductors. 2D Mater. 2017, 4, 021019.
- (26) Peyskens, F.; Chakraborty, C.; Muneeb, M.; Van Thourhout, D.; Englund, D. Integration of single photon emitters in 2D layered materials with a silicon nitride photonic chip. *Nat. Commun.* **2019**, *10*, 4435.
- (27) Cai, T.; Dutta, S.; Aghaeimeibodi, S.; Yang, Z.; Nah, S.; Fourkas, J. T.; Waks, E. Coupling emission from single localized defects in two-dimensional semiconductor to surface plasmon polaritons. *Nano Lett.* **2017**, *17*, 6564–6568.
- (28) Kern, J.; Niehues, I.; Tonndorf, P.; Schmidt, R.; Wigger, D.; Schneider, R.; Stiehm, T.; Vasconcellos, S. M.; Reiter, D. E.; Kuhn, T.; Bratschitsch, R. Nanoscale positioning of single-photon emitters in atomically thin WSe<sub>2</sub>. Adv. Mater. **2016**, 28, 7101–7105.
- (29) Luo, Y.; Shepard, G. D.; Ardelean, J. V.; Rhodes, D. A.; Kim, B.; Barmak, K.; Hone, J. C.; Strauf, S. Deterministic coupling of site-controlled quantum emitters in monolayer WSe<sub>2</sub> to plasmonic nanocavities. *Nat. Nanotechnol.* **2018**, *13*, 1137–1142.
- (30) Linhart, L.; Paur, M.; Smejkal, V.; Burgdörfer, J.; Mueller, T.; Libisch, F. Localized intervalley defect excitons as single-photon emitters in WSe<sub>2</sub>. *Phys. Rev. Lett.* **2019**, *123*, 146401.
- (31) Moon, H.; Grosso, G.; Chakraborty, C.; Peng, C.; Taniguchi, T.; Watanabe, K.; Englund, D. Dynamic exciton funneling by local strain control in a monolayer semiconductor. *Nano Lett.* **2020**, 20, 6791–6797.
- (32) Castellanos-Gomez, A.; Buscema, M.; Molenaar, R.; Singh, V.; Janssen, L.; van der Zant, H. S J; Steele, G. A Deterministic transfer of two-dimensional materials by all-dry viscoelastic stamping. 2D Mater. 2014. 1, 011002.
- (33) Tien, D. H.; Park, J.-Y.; Kim, K. B.; Lee, N.; Choi, T.; Kim, P.; Taniguchi, T.; Watanabe, K.; Seo, Y. Study of graphene-based 2D-heterostructure device fabricated by all-dry transfer process. ACS Appl. Mater. Interfaces 2016, 8, 3072–3078.
- (34) Luo, Y.; Liu, N.; Li, X.; Hone, J. C.; Strauf, S. Single photon emission in WSe<sub>2</sub> up 160 K by quantum yield control. 2D Mater. **2019**, *6*, 3.
- (35) Desai, S. B.; Seol, G.; Kang, J. S.; Fang, H.; Battaglia, C.; Kapadia, R.; Ager, J. W.; Guo, J.; Javey, A. Strain-induced indirect to direct bandgap transition in multilayer WSe<sub>2</sub>. *Nano Lett.* **2014**, *14*, 4592–4597.
- (36) Niehues, I.; Schmidt, R.; Drüppel, M.; Marauhn, P.; Christiansen, D.; Selig, M.; Berghäuser, G.; Wigger, D.; Schneider, R.; Braasch, L.; Koch, R.; Castellanos-Gomez, A.; Kuhn, T.; Knorr, A.; Malic, E.; Rohlfing, M.; Vasconcellos, S. M.; Bratschitsch, R. Straincontrol of exciton-phonon coupling in atomically thin semiconductors. *Nano Lett.* 2018, 18, 1751–1757.
- (37) Schmidt, R.; Niehues, I.; Schneider, R.; Drüppel, M.; Deilmann, T.; Rohlfing, M.; Vasconcellos, S. M.; Castellanos-Gomez, A.; Bratschitsch, R. Reversible uniaxial strain tuning in atomically thin WSe<sub>2</sub>. 2D Mater. **2016**, *3*, 021011.

- (38) Kumar, S.; Brotons-Gisbert, M.; Al-Khuzheyri, R.; Branny, A.; Ballesteros-Garcia, G.; Sanchez-Royo, J. F.; Gerardot, B. D. Resonant laser spectroscopy of localized excitons in monolayer WSe<sub>2</sub>. *Optica* **2016**. 3, 882–886.
- (39) Kim, H.; Moon, J. S.; Noh, G.; Lee, J.; Kim, J.-H. Position and frequency control of strain-induced quantum emitters in WSe<sub>2</sub> monolayers. *Nano Lett.* **2019**, *19*, 7534–7539.
- (40) Lee, J.; Karnadi, I.; Kim, J. T.; Lee, Y.-H.; Kim, M.-K. Printed nanolaser on silicon. ACS Photonics 2017, 4, 2117–2123.
- (41) Vahala, K. Optical microcavities. Nature 2003, 424, 839-846.
- (42) Rivera, P.; Fryett, T.; Chen, Y.; Liu, C.-H.; Ray, E.; Hatami, F.; Yan, J.; Mandrus, D.; Yao, W.; Majumdar, A.; Xu, X. Coupling of photonic crystal cavity and interlayer exciton in heterobilayer of transition metal dichalcogenides. 2D Mater. 2020, 7, 015027.
- (43) Ryu, H.-Y. Modification of internal quantum-efficiency and efficiency droop in GaN-based flip-chip light-emitting diodes via the Purcell effect. *Opt. Express* **2015**, 23, A1157–A1166.
- (44) Davanco, M.; Ates, S.; Liu, Y.; Srinivasan, K.  $Si_3N_4$  optomechanical crystals in the resolved-sideband regime. *Appl. Phys. Lett.* **2014**, *104*, 041101.